PAPER

Electron mobility and mode analysis of scattering for β-Ga$_2$O$_3$ from first principles

Electron mobility and mode analysis of scattering for $\beta-$Ga₂O₃ from first principles

Jinlong Ma[1,3] , **Fanchen Meng**[2], **Dongwei Xu**[1], **Run Hu**[1] and
Xiaobing Luo[1,3]

[1] School of Energy and Power Engineering, Huazhong University of Science and Technology, Wuhan 430074, People's Republic of China
[2] Department of Physics and Astronomy, Clemson University, Clemson, SC 29634, United States of America

E-mail: majinlong@hust.edu.cn and luoxb@hust.edu.cn

Abstract

The electrical transport properties of β-Ga₂O₃ are studied by first-principles calculations. The calculated intrinsic electron Hall mobilities agree well with experiments, with intrinsic Hall factor decreasing monotonically from 1.54 at 100 K to 1.14 at 800 K. The anisotropy of electron mobility is weak due to the almost isotropic electron effective mass, which also results in nearly isotropic Seebeck coefficient and electronic contribution to the thermal conductivity. The mode analysis of phonon scattering reveals that the optical phonon scattering is almost entirely determined by the long-range polar interactions, whereas the acoustic phonon scattering also plays an important role especially at low temperatures. The intrinsic electron mobility is significantly overestimated even above room temperature by only considering the polar optical phonon scattering, in contrast to previous predictions from fitting of phenomenological models.

(Some figures may appear in colour only in the online journal)

1. Introduction

β-Ga₂O₃ has attracted accelerated interest due to its promising application in electronic and photonic devices with capabilities beyond existing technologies [1]. The ultra-wide band gap (∼4.9 eV) [2] along with its transparent characteristic makes it an outstanding candidate for solar blind ultraviolet detector [3–5], and the photo-excitation gas sensor using ultraviolet-assisted β-Ga₂O₃ has also been demonstrated [6–8]. The exceptionally high Johnson and Baliga figures of merit advance the field of high-power/high-voltage devices which can overstep the performance of current Si, SiC and GaN based limits [9–11]. From the device application view-

point, the electrical and thermal transports of β-Ga₂O₃ are two fundamental but exceedingly important properties.

β-Ga₂O₃ has a highly anisotropic monoclinic crystal structure with $C2/m$ symmetry. Though early experiments reported strong anisotropy in electron mobility [12], later measurements have clarified that the mobility is nearly isotropic [13, 14] and the strong anisotropy found in early experiments is attributed to the twin boundaries in experimental samples [14]. Several sets of high-quality β-Ga₂O₃ single crystals have been experimentally measured [14–18], reporting a room-temperature electron Hall mobility of 130–176 cm² V⁻¹ s⁻¹. Phenomenological model analysis, by fitting the temperature dependence of experimental data, identifies that the dominant scattering mechanism changes from long-range polar optical phonon (POP) scattering caused by the strong coupling of electrons with longitudinal optical (LO) phonons to ionized

impurity scattering as temperature decreases [15–18]. The demarcation temperature decreases as the impurity concentration is reduced, reaching as low as 80 K in the purest samples [18] among previous experimental reports. By only considering the long-range electron–LO coupling in the complete phonon space for the phonon scattering, the effect of LO–plasmon interaction [19] and the presence of compensating impurity centers [20] are discussed. On the other hand, Parisini and Fornari [21] have systematically analyzed the scattering mechanisms in β-Ga$_2$O$_2$ and found that the nonpolar optical phonon (non-POP) scattering seems to be dominant above room temperature, but later they confirmed the crucial role of POP scattering by considering all LO modes [22].

Beyond the phenomenological analysis, the interactions between electrons and phonons can be directly obtained from density functional theory (DFT) and density functional perturbation theory (DFPT) calculations. Nonetheless, the computational cost is unbearable. Benefitting from the advances of Wannier interpolation of electron–phonon coupling matrix [23, 24], the first-principles calculations of electrical transport properties have been enabled in the framework of Boltzmann transport equations (BTEs), and the accuracy of this parameter-free method has been well verified [25–36]. Ghosh and Singisetti [37] have applied the first-principles calculations to study the electron mobility of β-Ga$_2$O$_3$ combined with ionized impurity scattering at a concentration of 1.1 ×10^{17} cm^{-3}, and observed a room-temperature drift mobility of 115 cm^2 V^{-1} s^{-1}. Nonetheless, the $40 \times 40 \times 40$ uniform meshes of the Brillouin zone are probably not enough for the convergence of electrical transport properties especially at low temperatures. Since the experimental record for the electron mobility of β-Ga$_2$O$_3$ is always refreshed, up to 176 cm^2 V^{-1} s^{-1} at room temperature in the latest measurement [18], the knowledge of the phonon-limited intrinsic upper limit of the electron drift and Hall mobilities of β-Ga$_2$O$_3$ is of great significance.

The thermal conductivity generally includes contributions from the electrons and the lattice. In the limit of weak doping, the electronic contribution to the thermal conductivity is negligible, and thus the lattice thermal conductivity of β-Ga$_2$O$_3$ has been experimentally measured, about 10–30 W m^{-1} K^{-1} at room temperature [38–40]. The first-principles calculation of lattice thermal conductivity, well developed in the past decades [41–45], has been applied to the study of β-Ga$_2$O$_3$, and provides good agreement with experiments [46]. In some technological applications, the β-Ga$_2$O$_3$ is intentionally doped, and thus the electronic contribution to the thermal conductivity may play a non-negligible role. The knowledge of the electronic contribution to the thermal conductivity as a function of carrier concentration is helpful to confirm this result.

Therefore, we calculated the intrinsic electrical transport properties of β-Ga$_2$O$_3$ by iteratively solving the BTE with scattering limited by electron–phonon coupling obtained from Wannier interpolation of DFT and DFPT calculations. The ionized impurity scattering was included for the cases involving doping effect. In this work, the electron effective mass is in good agreement with experiments; the convergence with

respect to the meshes of Brillouin zone is guaranteed; and the Hall factor is considered. Larger values of electron drift mobility than that reported in reference [37] are obtained and the calculated electron Hall mobilities agree well with the experimental measurements. The role of long-range polar interactions is quantitatively discussed by comparing the mobility calculated including full scatterings of phonons and that with only long-range POP scattering.

2. Methods

The evolution of electron occupation is described by BTE, from which the steady-state electrical transport properties can be derived [25, 26]. The electrical conductivity tensor is written as

$$\boldsymbol{\sigma} = \frac{2e^2}{\Omega N} \sum_{n\mathbf{k}} \mathbf{v}_{n\mathbf{k}} \mathbf{F}_{n\mathbf{k}} \left(-\frac{\partial f_{n\mathbf{k}}^0}{\partial \varepsilon_{n\mathbf{k}}} \right), \tag{1}$$

where e is the elementary charge, $n\mathbf{k}$ labels the electronic state with band index n and wave vector $\mathbf{k}$, Ω is the volume of unit cell, N is the number of meshes of Brillouin zone, $\mathbf{v}_{n\mathbf{k}}$ is the electron velocity, and $\mathbf{F}_{n\mathbf{k}}^0$ is the electron Fermi–Dirac occupation factor. Note that the factor 2 accounts for the spin degeneracy in spin-unpolarized calculations which otherwise should be 1. $\mathbf{F}_{n\mathbf{k}}$ is the mean free displacement of the electron state, and can be obtained by an iterative solution of BTE as [25]

$$\mathbf{F}_{n\mathbf{k}}^{i+1} = \tau_{n\mathbf{k}} \mathbf{v}_{n\mathbf{k}} + \tau_{n\mathbf{k}} \sum_{\mathbf{q}pm} \mathbf{W}_{n\mathbf{k},m\mathbf{k}+\mathbf{q}}^{\mathbf{q}p} \mathbf{F}_{m\mathbf{k}+\mathbf{q}}^{i}. \tag{2}$$

If neglecting the second term in the right side of equation (2), it is exactly the relaxation time approximation with $\mathbf{F}_{n\mathbf{k}}^0 = \tau_{n\mathbf{k}} \mathbf{v}_{n\mathbf{k}}$ and $\tau_{n\mathbf{k}}$ being the relaxation time. The transition probability by absorbing or emitting a phonon with wavevector $\mathbf{q}$ and mode index p is [25]

$$
\begin{aligned}
\mathbf{W}_{n\mathbf{k},m\mathbf{k}+\mathbf{q}}^{\mathbf{q}p} = & \frac{2\pi}{\hbar} |g_{n\mathbf{k},m\mathbf{k}+\mathbf{q}}^{\mathbf{q}p}|^2 \\
& \times \left[(n_{\mathbf{q}p}^0 + f_{m\mathbf{k}+\mathbf{q}}^0) \delta(\varepsilon_{n\mathbf{k}} + \hbar\omega_{\mathbf{q}p} - \varepsilon_{m\mathbf{k}+\mathbf{q}}) \right. \\
& \left. + (1 + n_{\mathbf{q}p}^0 - f_{m\mathbf{k}+\mathbf{q}}^0) \delta(\varepsilon_{n\mathbf{k}} - \hbar\omega_{\mathbf{q}p} - \varepsilon_{m\mathbf{k}+\mathbf{q}}) \right],
\end{aligned}
\tag{3}
$$

where $\varepsilon_{n\mathbf{k}}$ is the electron energy, $\omega_{\mathbf{q}p}$ is the phonon frequency, and $n_{\mathbf{q}p}^0$ is the phonon Bose–Einstein occupation factor. The electron–phonon coupling strength $g_{n\mathbf{k},m\mathbf{k}+\mathbf{q}}^{\mathbf{q}p}$ is calculated by [47]

$$g_{n\mathbf{k},m\mathbf{k}+\mathbf{q}}^{\mathbf{q}p} = \frac{1}{\sqrt{2\omega_{\mathbf{q}p}}} \langle \psi_{m\mathbf{k}+\mathbf{q}} | \partial V_{\mathbf{q}p} | \psi_{n\mathbf{k}} \rangle, \tag{4}$$

where $\partial V_{\mathbf{q}p}$ is the perturbation of the self-consistent potential due to lattice vibration [25], $\psi_{n\mathbf{k}}$ is the electronic wavefunction. In polar materials, the strong coupling strength with LO phonons in long wavelength cannot be correctly reproduced by the Wannier interpolation based on maximally localized Wannier functions [24]. To address this issue, a polar correction scheme is proposed [24, 48], in which the electron–phonon coupling matrix is divided into short-range and long-range parts, $g = g^S + g^L$. The short-range g^S is Wannier interpolated
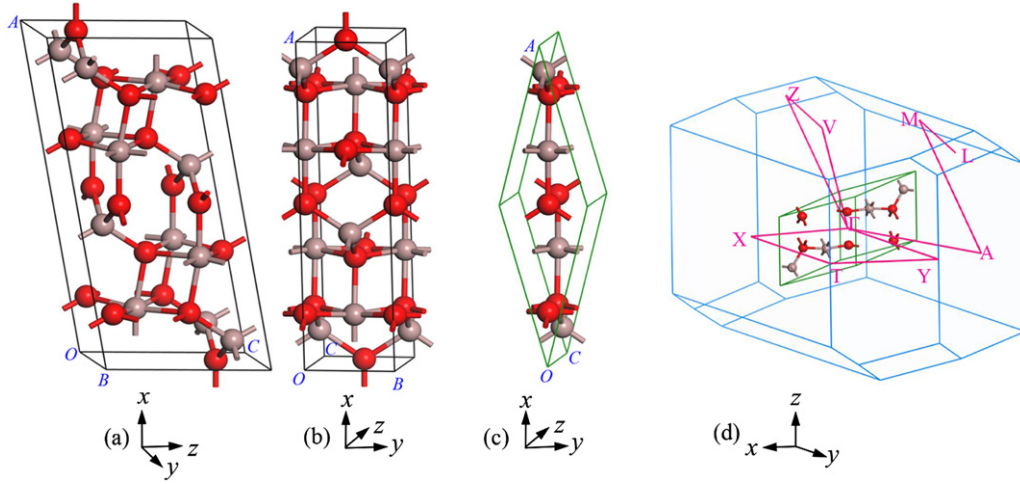
Figure 1. Conventional (a) and (b) and primitive (c) unit cell of β-Ga$_2$O$_3$ in the Cartesian space (red balls are Ga atoms and brown balls are O atoms). The primitive cell actually consists of the atoms in the AOC plane of the conventional cell. (d) The first Brillouin zone of the primite cell along with high-symmetry points in the Cartesian space.
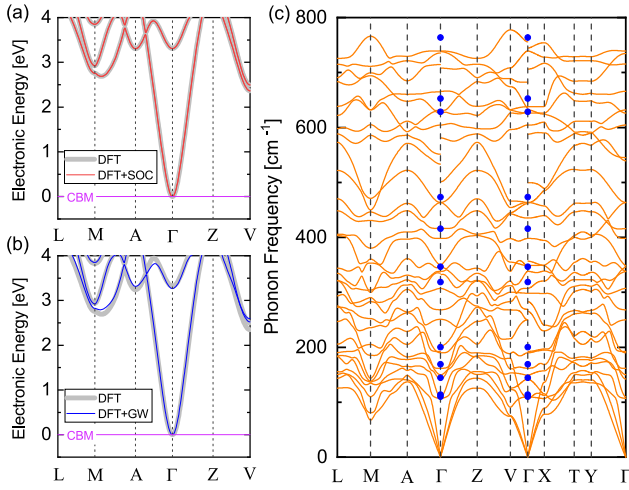
Figure 2. Band structures above the CBM of β-Ga$_2$O$_3$ calculated (a) with and without SOC, (b) with and without *GW* correction. (c) Phonon dispersion of β-Ga$_2$O$_3$ compared with the Raman measurements (blue dots) [60].

while the long-range g^L is analytically calculated from [24, 47, 48]

$$g_{n\mathbf{k},m\mathbf{k+q}}^{\mathbf{q}p,\mathrm{L}} = \frac{1}{\sqrt{2\omega_{\mathbf{q}p}}} \frac{i4\pi e^2}{\Omega\epsilon_0} \sum_{\mathbf{G}\neq\mathbf{q}} \frac{(\mathbf{q}+\mathbf{G})\cdot\mathbf{Z}^*\cdot\mathbf{e}_{\mathbf{q}p}}{(\mathbf{q}+\mathbf{G})\cdot\epsilon_\infty\cdot(\mathbf{q}+\mathbf{G})}$$
$$\times \left\langle \psi_{m\mathbf{k+q}} | e^{i(\mathbf{q}+\mathbf{G})\cdot\mathbf{r}} | \psi_{n\mathbf{k}} \right\rangle, \quad (5)$$

where $\mathbf{e}_{\mathbf{q}p}$ is the phonon eigenvector, $\mathbf{G}$ is the reciprocal lattice vector, $\mathbf{Z}^*$ is the Born effective charge, ϵ_0 is the vacuum permittivity, and ϵ_∞ is the high-frequency relative permittivity.

For doping cases, the ionized impurity scattering was considered using the Brooks and Herring model [49], in which the transition probability is given by

$$I_{n\mathbf{k},m\mathbf{k}'} = \frac{2\pi Z^2 n_c e^4}{\hbar\Omega(\epsilon_r\epsilon_0)^2} \cdot \frac{\delta(\varepsilon_{m\mathbf{k}'}-\varepsilon_{n\mathbf{k}})}{(\beta_s^2+|\mathbf{k}'-\mathbf{k}|^2)^2}, \quad (6)$$

where Z is the charge of the ionized impurity, n_c is the impurity concentration. Here, we simply assume that the doping is single donors which are fully ionized, thus $Z=1$ and n_c is equal to the carrier concentration. ϵ_r is the static relative permittivity, β_s is the inverse Thomas–Fermi screening length,

$$\beta_s^2 = \frac{n_c e^2}{\epsilon_r\epsilon_0 k_B T} \frac{F_{-1/2}(\eta)}{F_{1/2}(\eta)}, \quad (7)$$

where $F_j(\eta)$ is the Fermi–Dirac integral defined as [50]

$$F_j(\eta) = \int_0^\infty \frac{\xi^j}{1+\exp(\xi-\eta)} d\xi, \quad (8)$$

with $\xi = \varepsilon/k_B T$ and $\eta = \varepsilon_f/k_B T$ being the reduced energy and reduced chemical potential, respectively.

The scattering rate, the inverse of the relaxation time in equation (2), is computed by

$$\tau_{n\mathbf{k}}^{-1} = \sum_{\mathbf{q}pm} \mathbf{W}_{n\mathbf{k},m\mathbf{k+q}}^{\mathbf{q}p} + \sum_m I_{n\mathbf{k},m\mathbf{k}'}. \quad (9)$$

By dividing the conductivity with carrier concentration n_c, the mobility tensor is obtained as

$$\boldsymbol{\mu} = \frac{\boldsymbol{\sigma}}{en_c}. \quad (10)$$

The electronic contribution to the thermal conductivity is calculated as [26]

$$\boldsymbol{\kappa}_e = \frac{2}{T\Omega N} \sum_{n\mathbf{k}} (\varepsilon_{n\mathbf{k}}-\varepsilon_f)^2 \mathbf{v}_{n\mathbf{k}} \mathbf{F}_{n\mathbf{k}} \left(-\frac{\partial f_{n\mathbf{k}}^0}{\partial\varepsilon_{n\mathbf{k}}}\right) - T\boldsymbol{\sigma}\mathbf{S}^2, \quad (11)$$

where the Seebeck coefficient $\mathbf{S}$ can be obtained from [26]

$$\boldsymbol{\sigma}\mathbf{S} = \frac{2e}{T\Omega N} \sum_{n\mathbf{k}} (\varepsilon_{n\mathbf{k}}-\varepsilon_f) \mathbf{v}_{n\mathbf{k}} \mathbf{F}_{n\mathbf{k}} \left(-\frac{\partial f_{n\mathbf{k}}^0}{\partial\varepsilon_{n\mathbf{k}}}\right). \quad (12)$$

The mobility measured from Hall experiment differs from the calculated drift mobility of equation (10) by a Hall factor,

Table 1. Calculated phonon frequencies (in unit of cm^{-1}) of Raman active modes at Γ center compared with the Raman measurements. The diagonal components of the calculated high-frequency and static relative permittivity tensors ($\epsilon^x, \epsilon^y, \epsilon^z$) compared with previous calculations and experiments. The direction of the experimental values is not specified in references [63–65] whereas it is along the x-direction in reference [66].

	Phonon frequency			
Mode symmetry	Calculation	Experiment	Calculation	
	Present	Reference [60]	References [60]	References [59]
A_g	107	110.2	104	104.7
B_g	110	113.6	113	112.1
B_g	142	144.7	149	141.3
A_g	161	169.2	165	163.5
A_g	190	200.4	205	202.3
A_g	332	318.6	317	315.8
A_g	338	346.4	346	339.7
B_g	349		356	348.3
A_g	398	415.7	418	420.2
A_g	463		467	459.4
B_g	501	473.5	474	472.8
A_g	604		600	607.1
B_g	626	628.7	626	627.1
A_g	632	652.5	637	656.1
A_g	739	763.9	732	757.7
ϵ_∞	(4.00, 4.38, 4.14)	3.61 [63] 3.60 [64] 3.57 [65]	(4.02, 4.13, 4.15) [20] (3.81, 4.08, 3.85) [59]	
ϵ_r	(10.88, 11.61, 14.02)	9.93 [63] 9.57 [64] 10.2 [66]	(11.88, 9.22, 12.61) [20] (10.84, 11.49, 13.89) [59]	

$\mu_H = r_H \mu$. Here, the Hall factor is assumed as an isotropic scalar, and is computed from [35]

$$r_H = \langle \tau^2 \rangle / \langle \tau \rangle^2, \tag{13}$$

where $\langle \tau \rangle$ is the energy-averaged scattering rate [35], which is equivalently calculated in the discrete numerical computation with a form for classical electron gas as

$$\langle \tau^a \rangle = \frac{\sum_{n\mathbf{k}} (\tau_{n\mathbf{k}})^a x^{3/2} e^{-x}}{\sum_{n\mathbf{k}} x^{3/2} e^{-x}}, \tag{14}$$

with $x = \varepsilon_{n\mathbf{k}}/k_B T$. The applicability of this expression to monoclinic β-Ga_2O_3 has already been verified [20, 21].

3. Results and discussion

The crystal structure of monoclinic β-Ga_2O_3 in the Cartesian space is shown in figure 1, where the conventional unit cell contains 20 atoms. In our calculation, we reduce such a large conventional cell to its primitive cell with 10 atoms. The structure was first relaxed using Quantum ESPRESSO package [51], employing norm-conserving pseudopotentials with Perdew–Burke–Ernzerhof exchange–correlation functional [52] and a plane-wave kinetic energy cutoff of 72 Ry. To compare with experiments, the optimized lattice parameters of the primitive cell were converted back to those of the conventional cell, which are OA = 12.26 Å, OB = 3.05 Å,

OC = 5.81 Å, $\theta = 103.7°$, in good agreement with experimental values of OA = 12.23 Å, OB = 3.04 Å, OC = 5.80 Å, $\theta = 103.7°$ [53]. Since the valence bands of β-Ga_2O_3 are almost flat, the effective mass of the hole is much larger than that of the electron [54, 55]. Although the hole effective mass fitted along a special direction can be relatively small [54], the large density of states and huddled valence bands lead to strong scattering phase space, suggesting worse transport properties of holes than those of electrons. Moreover, the practically used β-Ga_2O_3 is the n-type system. Therefore, we hereafter focus on the transport properties for electrons if not otherwise noted.

In view of the light atomic masses of Ga and O atoms, the spin–orbit coupling (SOC) was not included in the calculations. This is confirmed by the fact that the conduction band structures calculated with and without SOC are exactly identical, as shown in figure 2(a). Since it has been pointed out that the many-body interaction could alter the electrical transport properties due to the change of effective mass [31, 33], the one-shot GW correction was carried out using YAMBO code [56]. Figure 2(b) shows that the GW correction has almost no effect on the band structure in a wide energy range above the conduction band minimum (CBM), and thus the GW correction was not included in the calculations. The CBM is located at the Γ point, and the energy-momentum dependence of this band valley is almost isotropic as previously reported [20, 37, 54]. The fitted electron effective mass is about $m_e^* = 0.282\, m_e$,

in good agreement with experimental values [57, 58] as well as calculations with HSE hybrid functional [20, 54]. The harmonic interatomic force constants were calculated with $3 \times 3 \times 3$ **q** grids, and were used to obtain the phonon dispersion of β-Ga$_2$O$_3$. The non-analytical correction due to long-range polar interactions was added using the calculated high-frequency permittivities. There are 30 phonon modes in the primitive unit cell of β-Ga$_2$O$_3$, as shown in figure 2(c). The zone-center modes can be classified into A$_u$ + 2B$_u$ acoustic phonons and 10A$_g$ + 4A$_u$ + 5B$_g$ + 8B$_u$ optical phonons [59], in which the A$_g$ and B$_g$ optical phonons are Raman active and have been experimentally measured [60]. The calculated values herein agree well with the Raman measurements, with discrepancy smaller than 6%, as listed in table 1. The A$_u$ and B$_u$ optical modes are infrared active, and correspond to the polar LO phonons which would have strong scattering with electrons [20]. Since the frequency of LO mode is strongly dependent on the direction of phonon wave vector, Parisini *et al* [22] provide spherically averaged LO frequencies by fitting the LO scattering rates using an analytical model; therein, the corresponding averaged coupling constants of each LO modes are also given. The coupling constant is proportional to the Callen effective charge, which is actually the Born effective charge divided by the high-frequency permittivity [61]. The static permittivities are obtained by the sum of the high-frequency permittivity and the contribution from zone-center polar modes [62]. The calculated permittivity of β-Ga$_2$O$_3$ is a tensor defined by the Cartesian directions in figure 1. The diagonal components of the high-frequency and static permittivity tensors are listed in table 1. Although the direction information of the crystal in reference [59] is not directly provided, it is justified to speculate that the same definition as this work was used in reference [59], since the lattice parameters, the high-symmetry points and the corresponding phonon dispersions along the *L–M–A–Γ–Z–V* are consistent. In addition, the crystal information in reference [20] indicates that the direction dependence of the permittivity therein is essentially equivalent to this work, although different high-symmetry lines, unfortunately not being illustrated therein, were chosen to display the phonon dispersion. Therefore, the sequence of the diagonal components of the permittivity tensors in references [20, 59] and this work should be the same, and they are in reasonable agreement with each other. The small discrepancy probably comes from the different pseudopotentials and parameters used in the calculations. For possible experimental measurements of the phonon dispersion of β-Ga$_2$O$_3$ in the future, which is more conveniently defined by the directions based on the conventional cell, the phonon dispersion relations along some special lines of the Γ–X, Γ–Y, and Γ–V are additionally given. The Γ–X and Γ–Y are parallel to the *x*- and *y*-directions in the real space, respectively, whereas the Γ–V is at an angle of 13.7° to the *z*-direction; thus, they are exactly corresponding to the directions perpendicular to the BOC, AOC and AOB planes of the conventional cell, respectively. In the experimental studies, the measurements do not provide all components of the permittivity tensor [63–66]; nonetheless, the measured values are close to the calculations herein and references [20, 59].
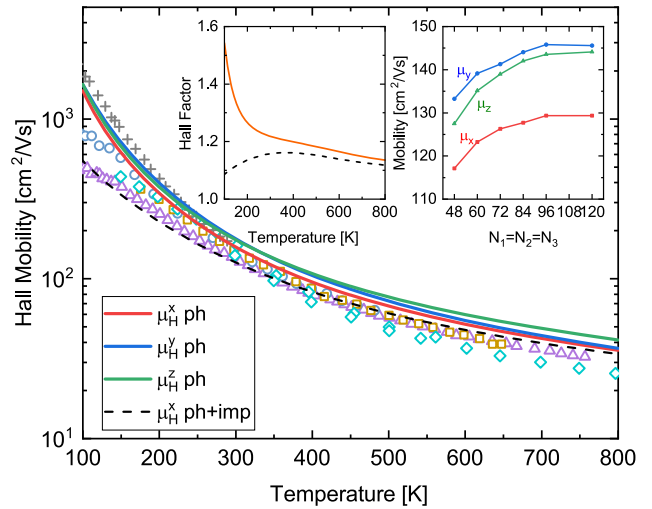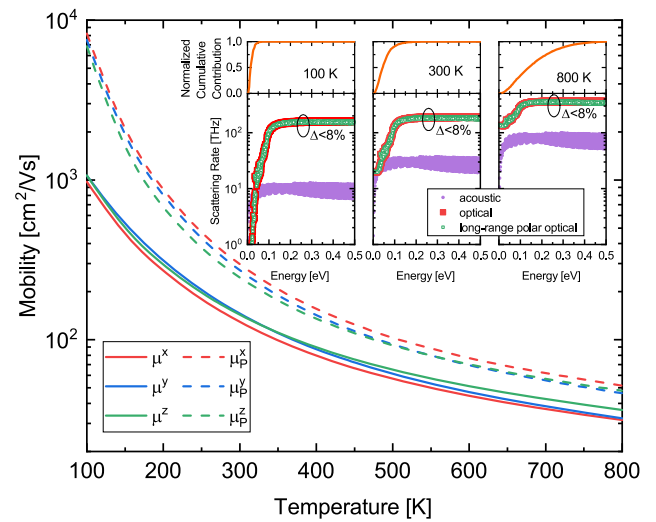

Figure 3. Calculated phonon-limited intrinsic electron Hall mobilities of β-Ga$_2$O$_3$ at different temperatures (solid lines). The values along the *x*-direction including both phonon and ionized impurity scatterings are also given for representative comparison (dashed line). Symbols are experimental values with triangles from reference [14], circles from reference [15], squares from reference [16], diamonds from reference [17], and crosses from reference [18]. The right inset shows the room-temperature electron drift mobilities as a function of **k** and **q** meshes of $N_i(\mathbf{k}) = N_i(\mathbf{q})$ with i being the three directions. The left inset gives the phonon-limited intrinsic Hall factor for electrons (solid line) and that including both phonon and ionized impurity scatterings (dashed line) at different temperatures.

To calculate electron mobility, the electron–phonon coupling matrix was first calculated on $6 \times 6 \times 6$ **k** and $3 \times 3 \times 3$ **q** grids. Then a framework combining the Wannier interpolation for the short-range part and analytical correction for the long-range part as implemented in the EPW package [47] was used to interpolate the electron–phonon coupling elements to dense grids. The convergence of electron mobility with respect to **k** and **q** meshes was checked and is shown in the inset of figure 3. It can be seen that the calculated mobilities reach convergence at $96 \times 96 \times 96$ **k** and **q** grids, with the difference compared to the values at grids of $120 \times 120 \times 120$ smaller than 1% at 300 K. It is known that the lower the temperature is, the closer the energy of the electron that can be activated is to CBM, so in order to obtain convergent results, the meshes of Brillouin zone required in the calculations are also larger. We have checked that the convergence of calculations at 100 K becomes worse but still can be guaranteed within 5%. This implies that the $40 \times 40 \times 40$ grids used in reference [37] is not enough, and would underestimate the values especially for low temperatures. The room-temperature intrinsic electron drift mobilities are 129, 146, and 144 cm^2 V^{-1} s^{-1} in *x*, *y* and *z* directions respectively, which are 12%–27% larger than the calculated value in reference [37]. Figure 3 shows that the intrinsic electron Hall mobilities of β-Ga$_2$O$_3$ at different temperatures are in reasonable agreement with experimental results [14–18], with room-temperature values of 158, 178, and 175 cm^2 V^{-1} s^{-1} in *x*, *y* and *z* directions, respectively. It can be seen that the discrepancy between different experimental values is relatively

large at low temperatures, due to the effect of different ionized impurity scatterings which play a more important role at low temperatures [15, 16, 18, 21]. Among the experimental values plotted in figure 3, the carrier concentration in reference [18] is below 10^{16} cm^{-3}, while that of reference [14] is about 10^{17} cm^{-3}. When including ionized impurity scattering with a concentration of 1×10^{17} cm^{-3}, the calculated low-temperature values are decreased to good agreement with reference [14], whereas the high-temperature values are less affected. The remaining discrepancy between calculations and experiments can be attributed to the experimental measurement errors and the excluded effects of temperature-dependent band structures, inevitable sample-dependent defects, distortions or boundaries, and so forth. The Hall factors for electrons at different temperatures are calculated, as shown in the inset of figure 3. The intrinsic Hall factor decreases monotonically from 1.54 at 100 K to 1.14 at 800 K, whereas if the ionized impurity scattering is included, the Hall factor first increases and then decreases. The influence of scattering mechanisms on the Hall factor has already been revealed by Parisini and Fornari [21, 22]. The temperature dependence of the Hall factor including ionized impurity scattering agrees with the study of reference [22]. Since the phonon scattering dominates impurity scattering at high temperatures, it is not hard to understand the monotonic decrease of the intrinsic Hall factor.

The temperature dependent intrinsic electron drift mobilities are given in figure 4. It is found that the anisotropy of mobilities is not as strong as the anisotropy of crystal structure, within 15% in the temperature range of 100–800 K. This is attributed to the almost isotropic electronic valley around the Γ point. All electrons that participate in the transport below 800 K are located in this valley. The momentum conservation enforces the phonons acting with electrons also around the Γ point. As a consequence, the scattering from long-range POP is important because its coupling strength diverges as $1/|\mathbf{q}|$ for **q** approaching Γ [24, 48]. Previous qualitative analyses based on phenomenological models predict that the electron mobility above room temperature is almost entirely determined by the POP scattering [15, 16, 18]. However, we found that the mobilities limited only by POP scattering are about 1.7–2.3 times larger than the values including full scatterings of phonons at room temperature. The overestimation decreases as temperature increases, from 6–8 times at 100 K to 1.3–1.6 times at 800 K.

To understand the decrease of overestimation, we separate the scattering rates of acoustic and optical phonons, as shown in the inset of figure 4. It is noticed that the scattering rates of optical phonons are almost entirely contributed by the long-range POP interactions, more than 92% in the temperature range of 100–800 K. The normalized cumulative distribution, which is the mobility contributed by electrons below a specified energy divided by the total mobility, shows that more than 98% of the mobility is contributed by electrons below 0.05 eV at 100 K, and within this energy range, the acoustic phonons have much larger scattering rates than those of optical phonons. Therefore, consideration of only POP scattering would greatly underestimate the total scattering rates. As

Figure 4. Phonon-limited intrinsic electron drift mobilities calculated with full scatterings of phonons (solid lines) and long-range POP scattering only (dashed lines). The inset shows the scattering rates contributed from acoustic and optical phonons at different temperatures. The long-range POP scattering rates are provided for comparison, with the difference (Δ) compared to the optical phonon scattering rates smaller than 8%. The normalized cumulative contributions to the mobility from electrons at a given energy are also plotted.

temperature increases, the contribution from high-energy electrons increases, about 98% of the mobility being contributed by electrons with energies up to 0.15 eV at 300 K and 0.42 eV at 800 K. Meanwhile, the scattering of optical phonons becomes larger than acoustic phonons especially at low energies, due to its faster increase of occupation numbers [34] multiplied with stronger coupling strength of polar modes [24, 29, 48]. As a consequence, the relative contribution of optical phonons increases, and the deviation between long-range POP scattering rate and total scattering rate decreases, thus the overestimation of electron mobilities is reduced. Although the acoustic phonon scattering is regarded as negligible in previous phenomenological analyses [15, 16, 18] especially for doped β-Ga$_2$O$_3$ [20, 21], the entirely first-principles calculations herein indicate that the role of acoustic phonon scattering is important in intrinsically pure β-Ga$_2$O$_3$. Actually, this is not surprising since the non-negligible role of acoustic phonons has already been implied by Parisini and Fornari [21, 22]. In reference [22], it is highlighted that the scattering from acoustic phonons cannot be neglected in the transport analysis since the interaction between electrons and acoustic phonons is physically active. Moreover, in reference [21], by fully considering the scattering mechanisms from acoustic phonons, non-POPs, POPs, ionized impurities and neutral impurities, an important trend revealed by the fitting of different samples is that the acoustic phonon scattering becomes non-negligible as the impurity is reduced, and eventually becomes comparable with ionized impurity scattering and non-POP scattering in the temperature range of 100–300 K.

Figure 5(a) shows the carrier concentration dependence of electron Hall mobilities including phonon and ionized impurity scatterings at room temperature. The calculated results
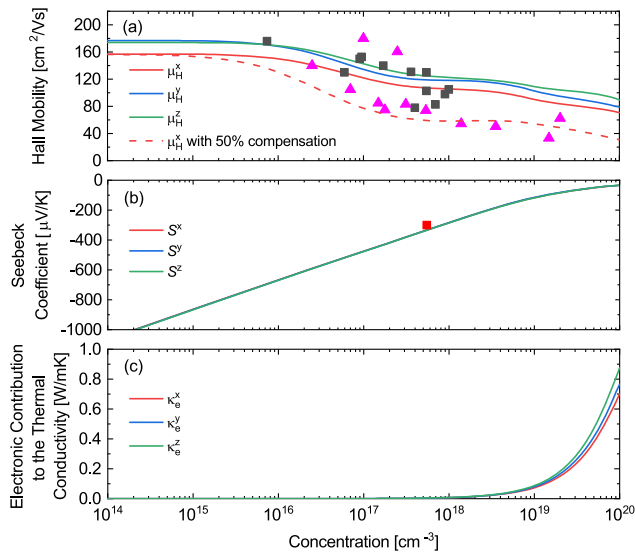
Figure 5. Carrier concentration dependence of (a) Hall mobilities, (b) Seebeck coefficients, and (c) electronic contribution to the thermal conductivities of β-Ga$_2$O$_3$ including phonon and ionized impurity scatterings at room temperature. The impurity concentration is assumed equal to the carrier concentration and the impurity charge is set to $Z = 1$. In (a) the experimental Hall mobilities are extracted from references [13–18, 67–70] (squares) and [71] (triangles), whereas in (b) the experimental Seebeck coefficient is obtained from reference [70].

agree well with the experimental data [13–18, 67–70] except the dispersed values in reference [71] which is probably owing to the presence of compensating sample-dependent defects [20]. It can be seen that the mobilities obviously decrease when the concentration exceeds 10^{16} cm^{-3}. This is slightly different from reference [20] which shows an increase of mobility as carrier concentration increases from 10^{17} to 10^{19} cm^{-3} without considering the impurity compensation. The increase of mobility stems from the suppression of long-range LO phonon scattering by the free-carrier screening effect [20], which is, however, not considered in our calculations herein. Nonetheless, the important role of impurity compensation emphasized in reference [20] is also found. Analogously with reference [20], we consider the Ga vacancies with $Z = 3$ for the compensation, and when we assume a 50% compensation ratio, the calculated electron Hall mobilities can agree with the experimental values of the heavily doped samples in reference [71], as shown in figure 5(a) where only the values along the *x*-direction are plotted as representative. The Seebeck coefficients at different carrier concentrations are also calculated, as shown in figure 5(b), which are almost isotropic because they are mostly determined by the electronic band structure [32, 72]. A recent experiment measured the Seebeck coefficients of different β-Ga$_2$O$_3$ films [70], which gives a relatively consistent room-temperature value about $-(300 \pm 20)$ μV K^{-1} at concentrations of $(5.5–6.0) \times 10^{17}$ cm^{-3}, whereas the calculated value herein is -330 μV K^{-1}. Figure 5(c) gives the room-temperature electronic contribution to the thermal conductivity, which is smaller than 0.1 W m^{-1} K^{-1} below 10^{19} cm^{-3} and 0.9 W m^{-1} K^{-1} below 10^{20} cm^{-3}. As compared to the lattice thermal conductivity (10–30 W m^{-1} K^{-1})

[38–40, 46], the electronic contribution is not significant. Nonetheless, it is obvious that the electronic contribution rises quickly with concentration increasing from 10^{19} to 10^{20} cm^{-3}, thus the electronic contribution can be expected to become important at higher carrier concentrations.

4. Conclusion

In summary, the electrical mobility, Seebeck coefficient and electronic contribution to the thermal conductivity of β-Ga$_2$O$_3$ are calculated from first principles. The intrinsic phonon scattering and ionized impurity scattering are considered. By taking into account the intrinsic Hall factor, which is about 1.54–1.14 in the temperature range of 100–800 K, the calculated intrinsic electron Hall mobilities can agree well with Hall experimental measurements. Different from the strongly anisotropic crystal structure, the anisotropy of electron mobility is within 15%, due to the almost isotropic electron effective mass around the CBM. The mode-dependent scattering rates indicate that the acoustic phonon scattering is comparable with long-range polar optical scattering for low-energy electrons. Therefore, acoustic phonons play a non-negligible role, in contrast to previous predictions of phenomenological models that the mobility is almost entirely determined by POPs above room temperature. After validating the concentration dependencies of the Hall mobility and Seebeck coefficient, which are in reasonable agreement with experiments, the electronic contribution to the thermal conductivities is calculated and found to be negligible as compared to the lattice thermal conductivity with carrier concentration below 10^{20} cm^{-3} at room temperature.

ORCID iDs

Jinlong Ma https://orcid.org/0000-0003-3009-2084
Run Hu https://orcid.org/0000-0003-0274-9982
Xiaobing Luo https://orcid.org/0000-0002-6423-9868

References

[1] Pearton S J, Yang J, Cary P H, Ren F, Kim J, Tadjer M J and Mastro M A 2018 *Appl. Phys. Rev.* **5** 011301
[2] Orita M, Ohta H, Hirano M and Hosono H 2000 *Appl. Phys. Lett.* **77** 4166
[3] Kokubun Y, Miura K, Endo F and Nakagomi S 2007 *Appl. Phys. Lett.* **90** 031912

[4] Xu J, Zheng W and Huang F 2019 *J. Mater. Chem.* C **7** 8753

[5] Chen X, Ren F, Gu S and Ye J 2019 *Photon. Res.* **7** 381

[6] Lin H J, Gao H and Gao P X 2017 *Appl. Phys. Lett.* **110** 043101

[7] Lin H J, Baltrus J P, Gao H, Ding Y, Nam C Y, Ohodnicki P and Gao P X 2016 *ACS Appl. Mater. Interfaces* **8** 8880

[8] Liu Z, Yamazaki T, Shen Y, Kikuta T, Nakatani N and Li Y 2008 *Sensors Actuators* B **129** 666

[9] Higashiwaki M, Sasaki K, Kuramata A, Masui T and Yamakoshi S 2012 *Appl. Phys. Lett.* **100** 013504

[10] Higashiwaki M, Sasaki K, Murakami H, Kumagai Y, Koukitu A, Kuramata A, Masui T and Yamakoshi S 2016 *Semicond. Sci. Technol.* **31** 034001

[11] Mastro M A, Kuramata A, Calkins J, Kim J, Ren F and Pearton S J 2017 *ECS J. Solid State Sci. Technol.* **6** P356

[12] Ueda N, Hosono H, Waseda R and Kawazoe H 1997 *Appl. Phys. Lett.* **71** 933

[13] Víllora E G, Shimamura K, Yoshikawa Y, Aoki K and Ichinose N 2004 *J. Cryst. Growth* **270** 420

[14] Irmscher K, Galazka Z, Pietsch M, Uecker R and Fornari R 2011 *J. Appl. Phys.* **110** 063720

[15] Oishi T, Koga Y, Harada K and Kasu M 2015 *Appl. Phys. Express* **8** 031101

[16] Ma N, Tanen N, Verma A, Guo Z, Luo T, Xing H G and Jena D 2016 *Appl. Phys. Lett.* **109** 212101

[17] Neal A T, Mou S, Lopez R, Li J V, Thomson D B, Chabak K D and Jessen G H 2017 *Sci. Rep.* **7** 13218

[18] Zhang Y, Alema F, Mauze A, Koksaldi O S, Miller R, Osinsky A and Speck J S 2019 *Apl Mater.* **7** 022506

[19] Ghosh K and Singisetti U 2017 *J. Mater. Res.* **32** 41422

[20] Kang Y, Krishnaswamy K, Peelaers H and Van de Walle C G 2017 *J. Phys.: Condens. Matter* **29** 234001

[21] Parisini A and Fornari R 2016 *Semicond. Sci. Technol.* **31** 035023

[22] Parisini A, Ghosh K, Singisetti U and Fornari R 2018 *Semicond. Sci. Technol.* **33** 105008

[23] Noffsinger J, Giustino F, Malone B D, Park C H, Louie S G and Cohen M L 2010 *Comput. Phys. Commun.* **181** 2140

[24] Verdi C and Giustino F 2015 *Phys. Rev. Lett.* **115** 176401

[25] Li W 2015 *Phys. Rev.* B **92** 075405

[26] Qiu B, Tian Z, Vallabhaneni A, Liao B, Mendoza J M, Restrepo O D, Ruan X and Chen G 2015 *Europhys. Lett.* **109** 57006

[27] Zhou J, Liao B, Qiu B, Huberman S, Esfarjani K, Dresselhaus M S and Chen G 2015 *Proc. Natl Acad. Sci.* **112** 14777

[28] Fiorentini M and Bonini N 2016 *Phys. Rev.* B **94** 085204

[29] Zhou J J and Bernardi M 2016 *Phys. Rev.* B **94** 201201(R)

[30] Liu T H, Zhou J, Liao B, Singh D J and Chen G 2017 *Phys. Rev.* B **95** 075206

[31] Ma J, Nissimagoudar A S and Li W 2018 *Phys. Rev.* B **97** 045201

[32] Ma J, Chen Y and Li W 2018 *Phys. Rev.* B **97** 205207

[33] Poncé S, Margine E R and Giustino F 2018 *Phys. Rev.* B **97** 121201(R)

[34] Meng F, Ma J, He J and Li W 2019 *Phys. Rev.* B **99** 045201

[35] Poncé S, Jena D and Giustino F 2019 *Phys. Rev.* B **100** 085204

[36] Li S, Tong Z and Bao H 2019 *J. Appl. Phys.* **126** 025111

[37] Ghosh K and Singisetti U 2016 *Appl. Phys. Lett.* **109** 072102

[38] Galazka Z *et al* 2014 *J. Cryst. Growth* **404** 184

[39] Guo Z *et al* 2015 *Appl. Phys. Lett.* **106** 111909

[40] Handwerg M, Mitdank R, Galazka Z and Fischer S F 2015 *Semicond. Sci. Technol.* **30** 024006

[41] Li W, Carrete J, Katcho N A and Mingo N 2014 *Comput. Phys. Commun.* **185** 1747

[42] Togo A, Chaput L and Tanaka I 2015 *Phys. Rev.* B **91** 094306

[43] Broido D A, Malorny M, Birner G, Mingo N and Stewart D A 2007 *Appl. Phys. Lett.* **91** 231922

[44] Ward A, Broido D A, Stewart D A and Deinzer G 2009 *Phys. Rev.* B **80** 125203

[45] Ma J, Li W and Luo X 2014 *Phys. Rev.* B **90** 035203

[46] Santia M D, Tandon N and Albrecht J D 2015 *Appl. Phys. Lett.* **107** 041907

[47] Poncé S, Margine E, Verdi C and Giustino F 2016 *Comput. Phys. Commun.* **209** 116

[48] Sjakste J, Vast N, Calandra M and Mauri F 2015 *Phys. Rev.* B **92** 054307

[49] Chattopadhyay D and Queisser H J 1981 *Rev. Mod. Phys.* **53** 745

[50] Blakemore J 1982 *Solid State Electron.* **25** 1067

[51] Giannozzi P *et al* 2017 *J. Phys.: Condens. Matter* **29** 465901

[52] Perdew J P, Burke K and Ernzerhof M 1996 *Phys. Rev. Lett.* **77** 3865

[53] Geller S 1960 *J. Chem. Phys.* **33** 676

[54] Varley J B, Weber J R, Janotti A and Van de Walle C G 2010 *Appl. Phys. Lett.* **97** 142106

[55] Yamaguchi K 2004 *Solid State Commun.* **131** 739

[56] Marini A, Hogan C, Gruning M and Varsano D 2009 *Comput. Phys. Commun.* **180** 1392–403

[57] Mohamed M *et al* 2010 *Appl. Phys. Lett.* **97** 211903

[58] Janowitz C *et al* 2011 *New J. Phys.* **13** 085014

[59] Liu B, Gu M and Liu X 2007 *Appl. Phys. Lett.* **91** 172102

[60] Machon D, McMillan P F, Xu B and Dong J 2006 *Phys. Rev.* B **73** 094125

[61] Chang Y C and James R B 1996 *Phys. Rev.* B **53** 14200

[62] Fennie C J and Rabe K M 2003 *Phys. Rev.* B **68** 184111

[63] Passlack M, Hunt N E J, Schubert E F, Zydzik G J, Hong M, Mannaerts J P, Opila R L and Fischer R J 1994 *Appl. Phys. Lett.* **64** 2715

[64] Schmitz G, Gassmann P and Franchy R 1998 *J. Appl. Phys.* **83** 2533

[65] Rebien M, Henrion W, Hong M, Mannaerts J P and Fleischer M 2002 *Appl. Phys. Lett.* **81** 250

[66] Hoeneisen B, Mead C and Nicolet M A 1971 *Solid State Electron.* **14** 1057

[67] Vllora E G, Shimamura K, Ujiie T and Aoki K 2008 *Appl. Phys. Lett.* **92** 202118

[68] Galazka Z *et al* 2010 *Cryst. Res. Technol.* **45** 1229

[69] Hwang W S *et al* 2014 *Appl. Phys. Lett.* **104** 203111

[70] Boy J, Handwerg M, Ahrling R, Mitdank R, Wagner G, Galazka Z and Fischer S F 2019 *Apl Mater.* **7** 022526

[71] Sasaki K, Kuramata A, Masui T, Villoran E G, Shimamura K and Yamakoshi S 2012 *Appl. Phys. Express* **5** 035502

[72] Dewandre A, Hellman O, Bhattacharya S, Romero A H, Madsen G K H and Verstraete M J 2016 *Phys. Rev. Lett.* **117** 276601